Journal of Inorganic and Organometallic Polymers and Materials
https://doi.org/10.1007/s10904-024-03315-w

RESEARCH

A DFT Calculations of Mechanical, Optoelectronic and Transport Properties of Cubic $AMgI_3$ (A = Li/Na) Halides for Photovoltaic and Energy Conversion Applications

Mumtaz Manzoor[1] · **Anurag Tewari**[2] · **Sabah Ansar**[3] · **Yedluri Anil Kumar**[4] · **Ramesh Sharma**[5]

Received: 20 June 2024 / Accepted: 28 July 2024

Abstract

Due to their rich and extraordinary properties, halide perovskites have gained attention over time for their applications in thermoelectric and solar cells. This paper investigates the properties of cubic halides $AMgI_3$ (A = Li/Na) compounds focusing on their optoelectronic and thermoelectric characteristics using the FP-LAPW method and semi-classical Boltzmann transport theory. The structural (− 43130.389030 Ry, − 43440.262047 Ry) and mechanical stability were confirmed by assessing the tolerance factor (0.81, 0.87) and formation energy (−326.60, −76.38), and by evaluating the elastic constants, respectively. The calculated value of Poisson ratio and Pugh ratio greater than their cutoff limit (2.29 and 2.18) reveal that our examined materials are ductile in nature. To examine the optoelectronic and transport properties the Trans-Bhala modified Becke Johnson potential (TB–mBJ) is employed. Using the TB–mBJ exchange−correlation potential function, the calculated indirect band gap values for $LiMgI_3$ and $NaMgI_3$ are 2.56 and 2.71 eV, respectively. These band gaps are suitable for solar energy harvesting due to their broad optical absorption ranging from infrared to visible light. To look at how individual atoms contributed, the partial and total densities of states were calculated. To investigate the possible application in renewable energy devices, we lastly compute the thermo-electric parameters, such as thermal (κ/τ) and electricity (σ/τ) conductivity, the Seebeck coefficient (S), energy factor (PF), and figure of merit (zT), which were analysed by BoltzTraP code within a range of temperatures (300 K–600 K) and chemical potentials.

Keywords Solar cells · Alkali perovskites · UV and visible light · Mechanical stability · Thermoelectric qualities

1 Introduction

The exploration of new materials possessing essential functionalities has the potential to revolutionize various fields including nanotechnology [1, 2], computer technology [3, 4], solar energy [5, 6] and spintronics [7, 8]. With the vast number of distinct elements present in the periodic table, each capable of forming diverse crystal structures, there remain numerous unexplored semiconducting materials that could emerge as promising candidates for energy sources [9, 10], show casing remarkable multifunctional capabilities [11, 12]. Lead Li/Na-based perovskite halides are one of these; their novel uses in photovoltaics have attracted a lot of attention [13]. When compared to conventional thin-film solar cells, these Li/N-based perovskite the halides have shown better performance in laboratory settings [8, 14]. Li/Na-based perovskite halides have made amazing progress, as seen by their efficiency rising from 3.8% in 2009 to 22.7% in 2017 [9–12]. Li/Na-based perovskites halides exhibit

---

✉ Mumtaz Manzoor
mumtazmanzoor95@gmail.com

✉ Ramesh Sharma
sharmadft@gmail.com

[1] Institute of Physics, Slovak Academy of Science, Dubravska Cesta 9, Bratislava 84507, Slovakia

[2] Department Basic Science and Humanities, Pranveer Singh Institute of Technology, Kanpur 209305, U.P, India

[3] Department of Clinical Laboratory Sciences, College of Applied Medical Sciences, King Saud University, P.O. Box 10219, Riyadh 11433, Saudi Arabia

[4] Saveetha School of Engineering, Saveetha Institute of Medical and Technical Sciences, Saveetha University, Chennai 602105, Tamil Nadu, India

[5] Department of Applied Science, Feroze Gandhi Institute of Engineering and Technology, Raebareli 229001, Uttar pradesh, India

outstanding photovoltaic performance, which can be due to their unique properties such as defect tolerance, low exciton binding energies, favorable effective hole and electron masses, a good direct bandgap, and strong optical absorption [13, 15]. Li/Na-based perovskite halides have exceptional optoelectronic properties, which makes them extremely appropriate to produce solar cell devices [14–16]. Despite their widespread applicability, Li/Na-based perovskites have some drawbacks that prevent their large-scale commercialization [19, 20]. These drawbacks include unstable in the presence of moist [17, 18], light, heat, and toxicity. As a result, a lot of work has gone into investigating materials free of lead for optoelectronic uses [16]. Thus, it is crucial to reduce or completely remove leads from photovoltaic (PV) equipment [17, 21]. Therefore, it is necessary to discover safe and reliable new energy technologies [18, 19]. To solve this kind of problem, perovskite materials (ABX_3) [20] having the characteristics of photovoltaics (PV) that are most solar class technology [21–23], due to their significant properties [24, 25] and contribute to the production of the clean energy from pollution [26]. The most promising solar energy in the recent years has been organic–inorganic halide perovskite (OIHP) based PV technologies, which are efficient, inexpensive, and have special optoelectronic effects. However, the lower stability of OIHP performance was the main issue for solar cell production. For example, conventional OIHP like $MAPbI_3$ [27] and $MAPbX_3$ (X = Cl, Br, and I) [28, 29] have garnered considerable interest for their high efficiency and suitability for optoelectronic applications, despite concerns regarding their instability and the toxicity associated with the presence of lead (Pb)[30]. Most of the metal halide Pb-free materials [31] such as $ZYbI_3$ (Z = Rb, Cs) were used as perovskite materials as a result of their high competence efficiency [32]. Mahmood et al. [33] reported the narrow direct band structures with the band gap of 1.22 eV and 1.12 eV for $RbYbI_3$ and $CsYbI_3$, respectively, which are considered finest for solar cells. Interestingly, Ray et al. [34] proposed substituting divalent atoms (such as Ge, Sn, Pb, Mg, Ca, Sr, and Ba) for Pb to address the toxicity concerns associated with perovskite materials in photovoltaic applications [35]. They found that Mg and Ba perovskites are improbable to form in the cubic, tetragonal, or orthorhombic phases due to their positive formation energies [36]. While Ca and Sr perovskites exhibit negative formation energies with respect to the metal-iodide precursors, they possess wide band gaps, making them less favourable candidates for use in photovoltaic devices [37]. They additionally reported that the predictive capability of a local density functional with a non-separable gradient approximation (NGA) closely resembles that of hybrid functional in terms of band gap predictions, particularly when M in $CsMI_3$ represents a p-block element such as Pb, Sn, or Ge. The stability of perovskites material was identified to be enhanced by introducing K and Rb atoms [38], specifically, $KGeX_3$ and $RbGX_3$ (where X = Cl or Br) structures. Due to their exceptional optoelectronic properties, which include a high static refractive index, low reflectivity, high absorption coefficient, and excellent stability they have been thoroughly investigated for their possible uses in solar energy and photoelectric systems [39]. Furthermore, they exhibit relatively low levels of toxicity. Additionally, $CsGeX_3$ (X = F, Cl, and Br) perovskite has been identified [40]as a promising candidate for optoelectronic applications, owing to its exceptional electronic, optical, thermoelectric, and tuneable band gap properties [41]. The electrical and optical properties of different cubic lead – free halide perovskites, $CsMgX_3$ (X = Cl and Br) compounds were studied [42]. Like these compounds, the cubic halide perovskite $CsBX_3$ (B = Sn, Ge, X = I, Br, Cl) compounds were also reported as suitable for optoelectronic energy devices [43]. Furthermore, recently a narrow band gap perovskite material such as $BaZrS_3$ [44] and $CsYbI_3$ [45], were reported [46].

As far as air knowledge goes, there isn't any material out there now that talks about the physical characteristics of hypothetical cubic halides $AMgI_3$ (A = Li/Mg). Because they make it easier to develop high-performance electronic devices and provide a better knowledge of the underlying physical features, materials with basic crystal structures, such cubic ones, have piqued the interest of the scientific community [47].

"Our objective/ motivation was to study this material theoretically, to simulate the physical properties, by employing the mBJ, to calculate the band gap, to attain the band gap in visible region, to analyze the maximum absorption, and to check the thermal efficiency, to use in the solar cell and thermal devices." This work aims to explore the structural, electrical, thermo-electric, and magnetic properties of ferromagnetic half-metallic $AMgI_3$ (A = Li/Mg) substances. Theoretical research holds great importance for the practical application of these substances and could potentially enable their utilization in devices that operate at elevated temperatures. We use the improved Becke-Johnson functional (mBJ) to compute these properties of $AMgI_3$ (A = Li/Mg), and the results agree with other theoretical evidence.

2 Method of Calculations

The full potential linearized augmented plane wave plus local orbital (FP-LAPW + lo) [47] method within the density functional theory DFT [48] is employed to evaluate the structural, electronic, and thermoelectric behaviour of $AMgI_3$ (A = Li/Na) compounds. The exchange correlation potential is implemented using the generalized gradient approximation (PBE-GGA) which is incorporated as a code within the WIEN2k software-package [49–51]. The ground state parameters are obtained by optimizing a fully relaxed structure using PBE-GGA and Murnaghan's equation of states is employed to fit the energy of the ground state [52]. Although, generalized gradient approximation (GGA) are effective in determining the lattice constant accurately but they fail to provide precise values of the band gap. This issue is addressed by employing TB-mBJ potential [53]. This technique involves averaging the lattice-constant values obtained from GGA approximations, thereby enhancing accuracy of calculated band gap values of the materials. The FP-LAPW + lo method provides a reliable approach for solving Kohn–Sham equation. This approach involves division of unit-cell in two regions. The 1st region represents the spherical core of the atom while 2nd region corresponds outer interstitial space. The angular-momentum is expanded up to 12 for the first region and specific muffin-tin radii are chosen to prevent charge leakage from the atom's core. The selected muffin-tin radii for Li, Na, Mg, I am 2.50, 2.50, 1.95, 2.05 and 1.71 Bohr respectively. The plane-wave cut-off approach is utilized for 2nd interstitial segment with $R_{MT} \times K_{max} = 8$, where K_{max} denotes the highest number of K and R_{MT} represents least muffin-tin radius. The modifies tetrahedron approach is applied with 10,000 K-points for integration of Brillouin zone to achieve self-consistency. The elastic properties are calculated by IRelast method, which is built-in Wien2k code. Finally, thermoelectric characteristics are evaluated with these modified structures implemented in BoltzTrap coding [54].

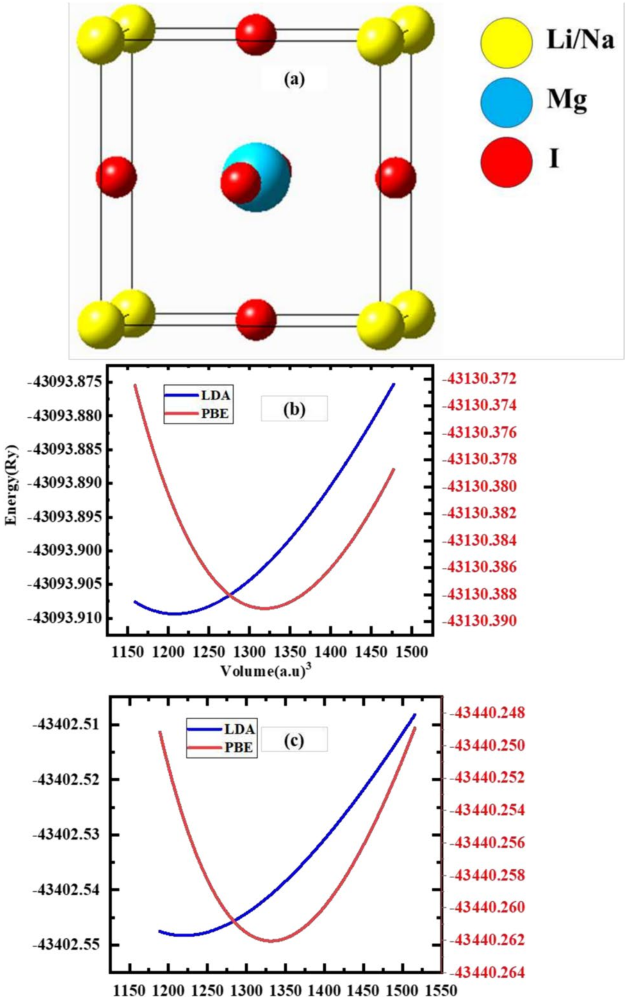

Fig. 1 Crystal structure of $AMgI_3$ (A = Li, Na) compounds and the LDA and GGA phases of $AMgI_3$ (A = Li, Na), along with their respective crystal structures and calculated total energy functions of a volume

3 Results and Discussion

3.1 Structural Analysis

For the calculations of structural properties, we used unit cell of cubic halides $AMgI_3$ (A = Li/Mg) with space group 221: Pm3m as shown in Fig. 1a. The cubic primitive unit cell of $AMgI_3$ (where A = Li/Na) comprises five atoms. A atoms are positioned at the corners in the 1a Wyckoff position (0, 0, 0), Mg atom occupy the body centre in the 1b Wyckoff position (0.5, 0.5, 0.5), and I atoms are positioned at the face centre in the Wyckoff position (0.5, 0.5, 0.0). The determination of structural characteristics of $AMgI_3$ (A = Li/Mg) compounds involves a volume optimization procedure. This involves optimizing the energy at specific volumes and fitting the resulting data points.

Goldschmidt tolerance factor denoted as "τ" is a widely used in the ABX_3 perovskite structures to investigate its structural stability. It insight to determine the compatibility of cations within the structure and is defined as follows [55]

$$t_G = \frac{(r_A + r_X)}{\sqrt{2}(r_B + r_X)} \tag{1}$$

where $r_{A,}$ r_{Mg}, and r_I are A − site, Mg − site, and I − site ionic radii, respectively. In general, perovskite structures are stable in cubic structure when the tolerance factor falls within the range of $0.8 < \tau < 1$ [56]. Alternatively, when $\tau < 0.8$, the perovskite adopts an orthorhombic structure, while for $\tau > 1$, it is categorized as having a hexagonal crystal structure [57]. The ionic radii used in this calculation were 1.13, 1.39, 0.72, and 2.20 Å, respectively, for Li, Na, Mg, and I. The calculated tolerance factors 0.81 for $LiMgI_3$ and 0.87 for $NaMgI_3$ are fall within an acceptable range as listed in Table 1, resulting in the confirming of the ideal cubic structural stability of the investigated compounds. Further material stability checked by the formation energy and cohesive energy.

Table 1 Calculated lattice constants (*a*), cell volume (*V*), ground state energy (E_o), bulk modulus (*B*) and Pressure Derivative of *B* (*B.P*), bond length, Cohesive energy and formation energies of cubic $AMgI_3$ (A = Li, Na)

Compound	XC	a (Å)	V(a.u^3)	B (GPa)	B_P	E_{tot}(Ry)	E_c (eV/atom)	E_f (KJ/mol)	Bader charges
$LiMgI_3$	LDA	5.63	1207.79	23.83	4.32	−43093.909352	1.75	−326.60	Li = 0.95 Mg = 1.44 I = − 0.79
	PBE	5.80	1318.24	19.62	4.76	−43130.389030			
	Ref								
NaMgI3	LDA	5.65	1219.33	25.44	5.13	−43402.548258	1.78	−76.38	Na = 0.89 Mg = 1.54 I = − 0.81
	PBE	5.82	1331.45	19.624	5.11	−43440.262047			
	Ref [69]	5.76	1318.64	22.45	5.03	−43095.3256	1.97	229.21	

The obtained cohesive energies and formation enthalpies are listed in Table 1. From Table 1, we can see that the cohesive energies and formation enthalpyy of all investigated compounds are negative, indicating that these materials are energetically stable. Table 1 shows a stable trend where, as one moves from Li to Na in the group, the lattice constantly rises and the bulk modulus falls. This is supported by the fact that as we proceed down the group, the atomic radius grows, expanding interatomic space. The bulk modulus decreases and the solid becomes less dense because of increased compressibility caused by the expansion of the atomic radius. The materials under investigation have a bandgap between 2.5 and 3.5 eV (1 eV = 1.602×10^{-19} Joules), which indicates that they are broad bandgap semiconductors.

Structural stability is also achieved by optimization to get ground state lattice parameters (−43130.389030 Ry, −43440.262047 Ry) as shown in Fig. 1b, c. The calculated parameters perfectly fit the Brich–Murnaghan equation of state.

$$E(V) = E + \frac{9B_0V_0}{16}\left\{\left[\left(\frac{V_0}{V}\right)^{2/3} - 1\right]B_0' + \left[\left(\frac{V_0}{V}\right)^{2/3} - 1\right]\left[6 - 4\left(\frac{V_0}{V}\right)^{2/3} - 1\right]\right\} \quad (2)$$

In the above expression B_0, E_0 V, V_0 and E(V) represents the bulk modulus, ground state energy, volume, equilibrium volume, and total energy, respectively. We can find the most stable structure by changing the crystal lattice's parameters using above Eq. 2.

3.2 Electron Localization Function (ELF)

The Electron Localization Function (ELF) serves as a valuable tool for analyzing electron distribution and localization during crystalline structure formation [47]. ELF quantifies the likelihood of electrons with identical spins and fixed positions within a reference electron field, offering insights into electron localization within the lattice space and revealing bonding characteristics in materials. Figure 2 presents 3D and 110 crystal dimension ELF maps for $AMgI_3$ (A = Li/Na). The right side of the ELF maps illustrates ELF scaling, including coordination scaling, where regions with lower electron density are depicted in blue and those with higher electron density in red. Examination of the ELF maps for compounds reveals a heightened degree of electron localization around the I ions, attributed to their significant electronegativity.

3.3 Band Structures and Density of States

The investigation of the band structure for the perovskite compound $AMgI_3$ (X = Li/Na) was semiconductor, the electronic band structure along some high symmetry directions of the BZ and their corresponding densities of states were calculated using the FP-LAPW method within the PBE-GGA and TB-mBJ functionals.

Table 2 reveal that narrow indirect band gaps were computed for $LiMgI_3$ and $NaMgI_3$ using GGA-PBE, and TB-mBJ. Specifically, the band gaps are 2.56 eV and 2.72 eV, respectively, for $LiMgI_3$ and $NaMgI_3$, employing GGA-PBE, and TB-mBJ. It's clear from that the PBE function consistently underestimates the electronic structure, particularly the band gap as shown in Fig. 3. Despite this underestimation, the results suggest that the proposed compounds exhibit sufficient stability, as they yield similar outcomes across different computational codes. Furthermore, the Tb-mBJ correlation function accurately predicts the band gap, correlating well with experimental values. This suggests that $LiMgI_3$ and $NaMgI_3$ have a favourable band gap which shows a potential engagement as a semiconductor material for use in PV devices. Figure 3a, b shows that both the conduction band minimum (CBM) and valance band maximum (VBM) of $LiMgI_3$ and $NaMgI_3$ compounds were located at Γ and M, respectively, in the first Brillion zone. Which agrees with the previous finding. The s-block valance band (VB) metals are flat between R and M points, suggesting the presence of

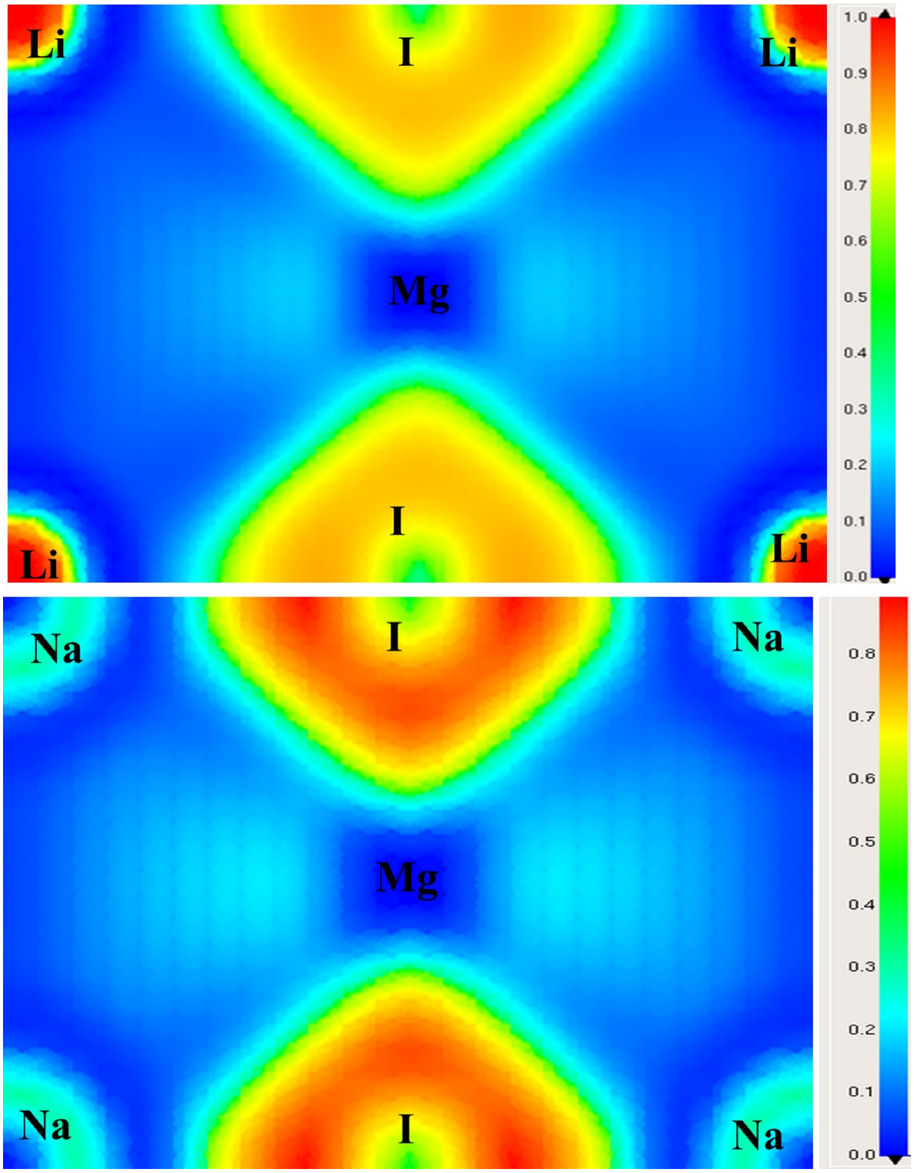

Fig. 2 ELF plot AMgI$_3$ (A = Li, Na)110 plane

Table 2 Calculated energy band gap (in eV) Mg based perovskite AMgI$_3$ (A = Li, Na) by different potentials PBE and mBJ

Properties	LDA (eV)	PBE (eV)	Tb-mBJ (eV)
LiMgI$_3$	1.071	1.340	2.555
NaMgI$_3$	1.072	1.337	2.714
Other work [28]			2.43

a heavy holes were observed, whereas the p-block metals have a more dispersive conduction band (CB) at $\Gamma-$point.

Figure 4 present the analysis of the partial density of states (PDOS) and total partial density of states (TDOS) of LiMgI$_3$ and NaMgI$_3$ compounds. Figure 4 illustrates the dominance of the Li s-state in the CB, situated away from the Fermi level. The proximity of the peak to the Fermi level is crucial for electron transitions from the VB to CB, despite the Li s-state's comparatively lower intensity near the Fermi level in the VB. In the case of the Mg atom, the s-state contributes to the VB, while the p-state contributes to the CB, as depicted in Fig. 4. Additionally, Fig. 4 clearly shows that the prominent peak near the Fermi level within the VB primarily originates from the Li p-state. In summary, the TDOS reveals that the VB is predominantly influenced by the Li p-state, whereas the Mg p-state contributes to the CB in the LiMgI$_3$ compound. Notably, when replacing Li atom with Na, similar trends are observed. These similarities arise from the shared properties of Li and Na as elements within the same family.

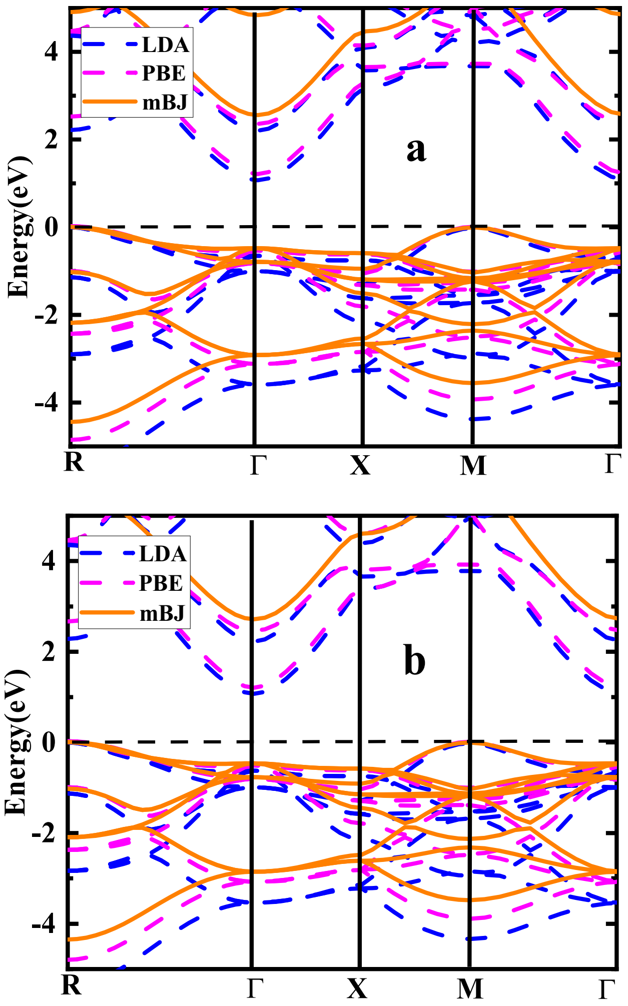

Fig. 3 The LDA, PBE-GGA and TB-mBJ approach was utilized in order to compute the band structure of **a** $LiMgI_3$ **b** $NaMgI_3$ in directions with good symmetry

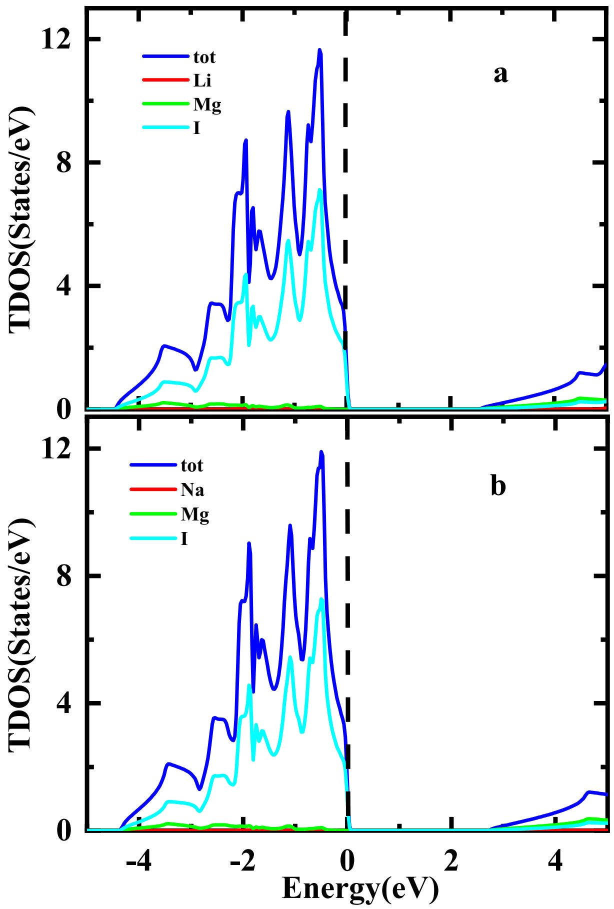

Fig. 4 TDOS and PDOS for $AMgI_3$ (A = Li, Na) computed using the TB-mBJ approximation

3.4 Elastic Properties

Elastic constants are needed to calculate mechanical characteristics, and the WIEN2k code's implementation of the IR-elast method yields these constants. Three elastic constants C_{11}, C_{12}, and C_{44} are sufficient to determine the mechanical properties of a cubic system. As far as we are aware, no report has been written about the mechanical characteristics of the materials under study. The cubic system must meet the following Born mechanical conditions to be stable: $C_{11} > 0$, $C_{44} > 0$, $C_{11} - C_{12} > 0$, $C_{11} + 2C_{12} > 0$, and $C_{11} > B > C_{12}$ [26]. According to Poisson's and Pugh's ratio, the calculated mechanical parameters, which are presented in Table 3, verified the mechanical stability of both $LiMgI_3$ and $NaMgI_3$. The following relations are used to compute the materials' elastic modulus for this purpose [58]. Interestingly, the estimated elastic constants of both $LiMgI_3$ and

Table 3 Calculated elastic constants (in GPa), anisotropy factor A, shear modulus G (in GPa), Young's modulus E (in GPa) and the Poisson ratio v of cubic indium-based perovskite $XMgI_3$ (X = Li, Na)

Parameters	$LiMgI_3$	$NaMgI_3$	Other work [18]
C_{11}	32.81	34.73	
C_{12}	12.57	12.70	17.09
C_{44}	7.44	8.14	7.75
B	19.32	20.04	21.45
S	8.41	9.191	10.66
Y	22.05	23.91	28.64
σ	0.309	0.301	
A	0.73	0.738	
B/G	2.29	2.18	
G/B	0.43	0.45	
C_p	5.13	4.56	
v_t	1550.52	1597.27	
v_l	2953.42	2994.39	
V_{avg}	1734.05	1784.37	
Θ_D	152.14	156.046	
T_m(K)	746.94	758.27	757.1

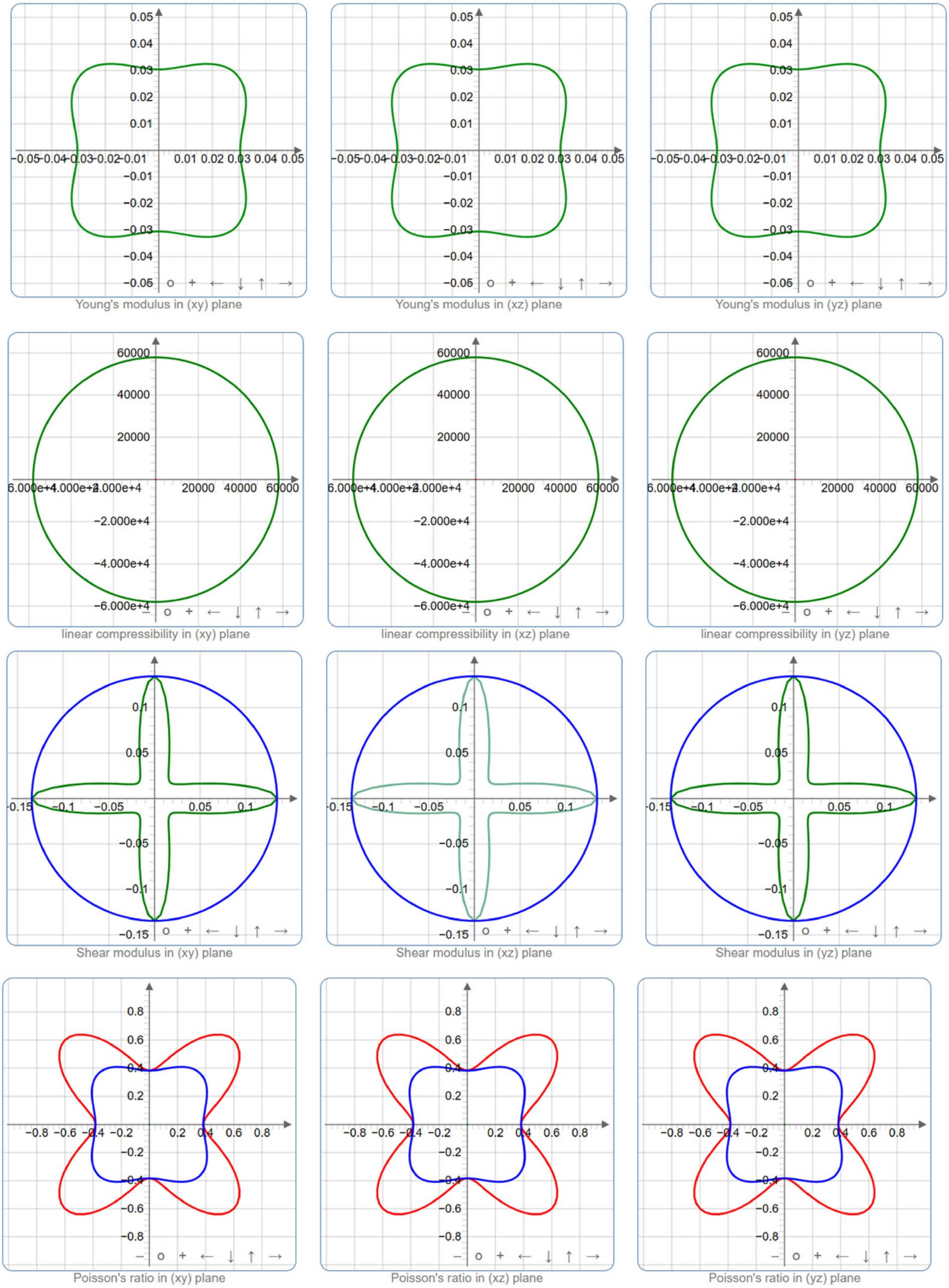

Young's modulus in (xy) plane
Young's modulus in (xz) plane
Young's modulus in (yz) plane
linear compressibility in (xy) plane
linear compressibility in (xz) plane
linear compressibility in (yz) plane
Shear modulus in (xy) plane
Shear modulus in (xz) plane
Shear modulus in (yz) plane
Poisson's ratio in (xy) plane
Poisson's ratio in (xz) plane
Poisson's ratio in (yz) plane

Fig. 5 3D and 2D elastic properties for $AMgI_3$ (A = Li, Na)

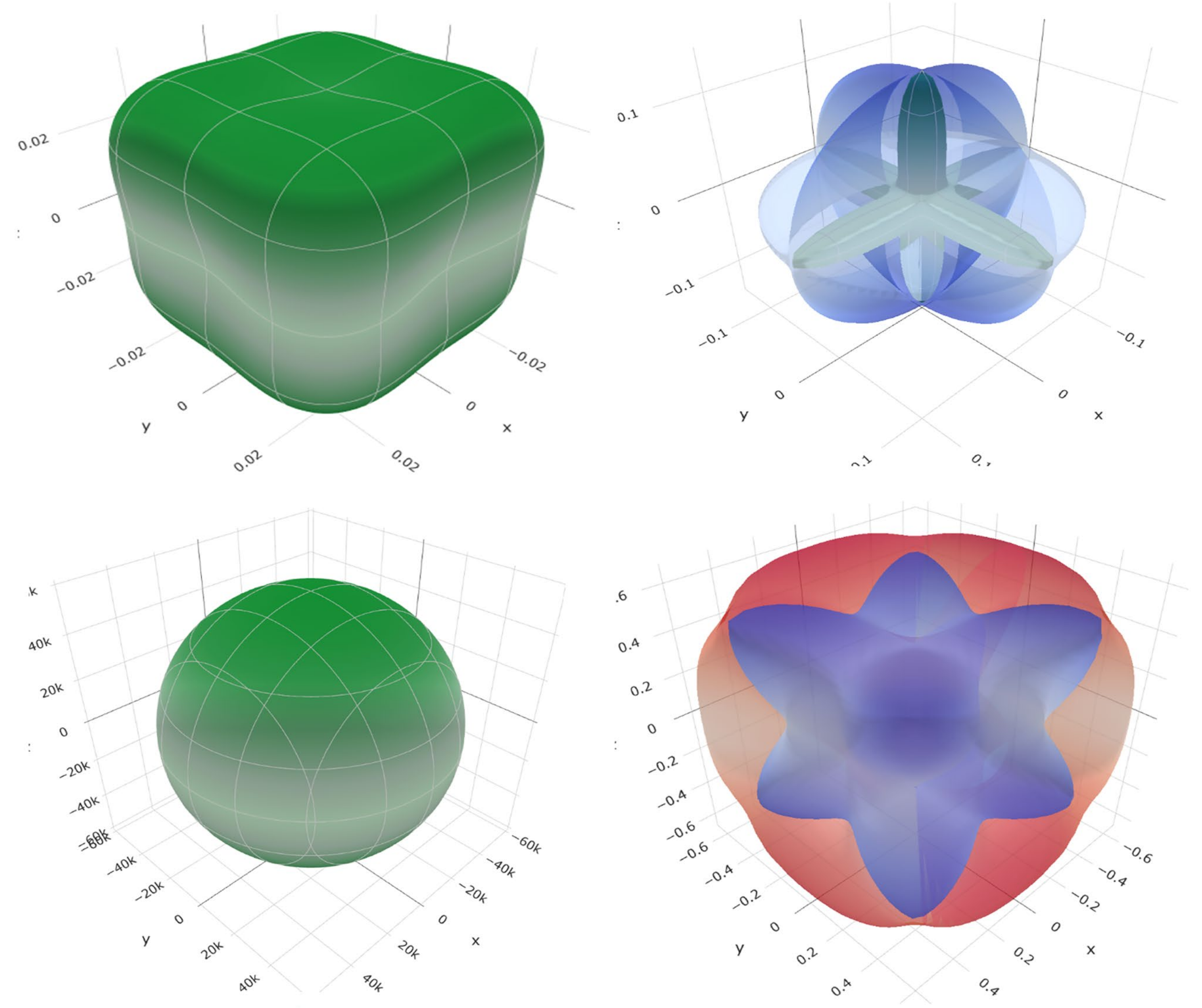

Fig. 5 (continued)

$NaMgI_3$ compounds listed in Table 3 confirmed that these compounds satisfy the Born stability criteria, indicating their mechanical stability. The Pugh ratio (B/G) and Cauchy pressure are useful parameters to assess a material's brittleness and ductility [59]. The ductility of the material is determined by B/G, which is equal to or greater than 1.75 whereas less than 1.75 represents the material's brittleness [60]. According to this study, the (B/G) ratios for $LiMgI_3$ (2.29) and $NaMgI_3$ (2.18) are higher than 1.75, suggesting that these materials exhibit ductile behaviour as shown in Table 3. The Cauchy pressure for cubic $LiMgI_3$ and $NaMgI_3$ determines their ductility and brittleness properties based on negative and positive values of C_{12}-C_{44}, as reported in [61]. The positive value indicates ductility while a negative value suggests brittleness. In this study, the difference between C_{12} and C_{44} for both compounds are positive values, resulting in indicating ductility. On the other hand, the Voigt-Reuss-Hill (VRH) method is an approach used to calculate B, G, E, and σ of the materials. The Voigt and Reuss methods are used to determine the bulk [62] and shear [63] moduli of materials, while Hill's [64] method is used to calculate the average values of these properties. The Reuss bulk modulus (B_R) and Voigt bulk modulus (B_V). all above computed parameters in 2D and 3D are shown in Fig. 5 for both compounds.

The values for B, G, and E are presented in Table 3. The B (19.32, 20.04), G (8.41, 9.19), and E (22.05, 323.91) of $AMgI_3$ (A = Li, Na), respectively, indicate that both materials exhibit comparable resistance to changes in volume and shape. Moreover, the observed E and σ listed in Table 3 can be calculated using the following expression, respectively [57]

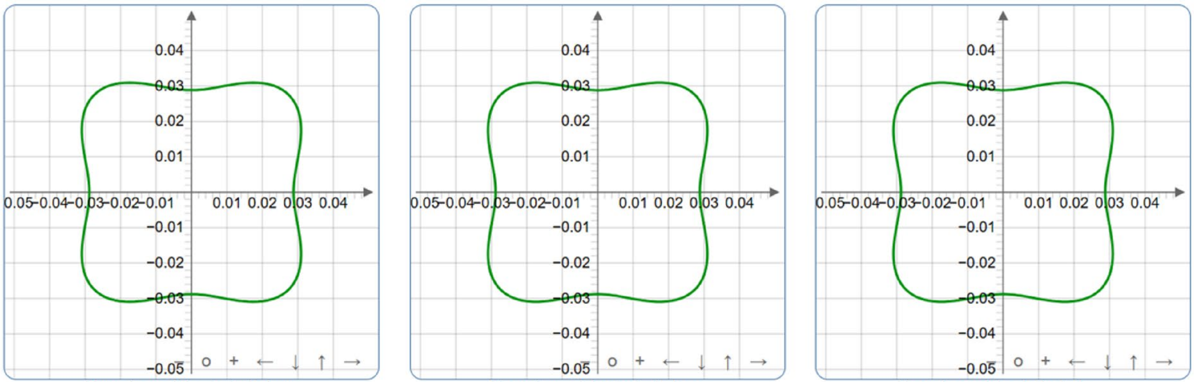

Young's modulus in (xy) plane Young's modulus in (xz) plane Young's modulus in (yz) plane

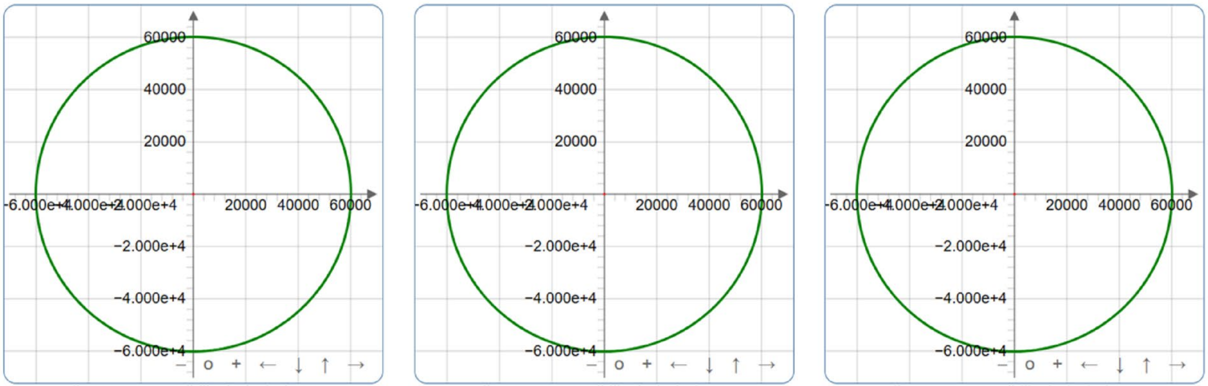

linear compressibility in (xy) plane linear compressibility in (xz) plane linear compressibility in (yz) plane

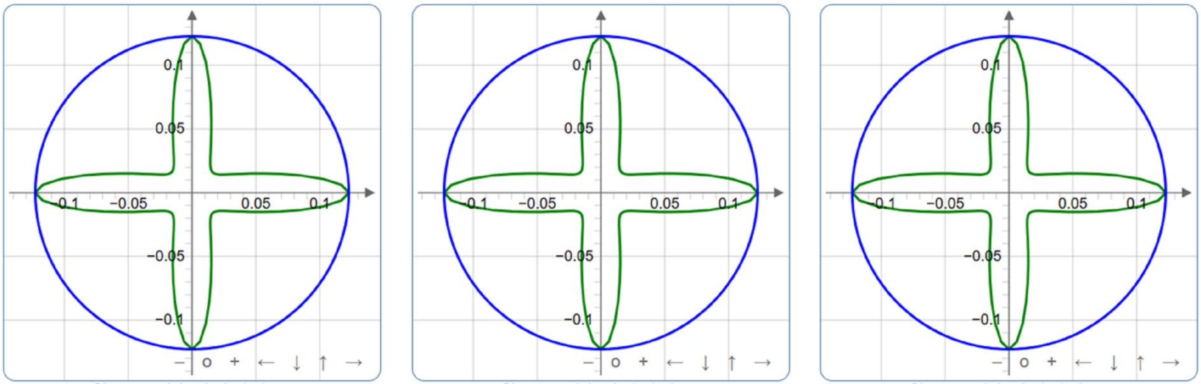

Shear modulus in (xy) plane Shear modulus in (xz) plane Shear modulus in (yz) plane

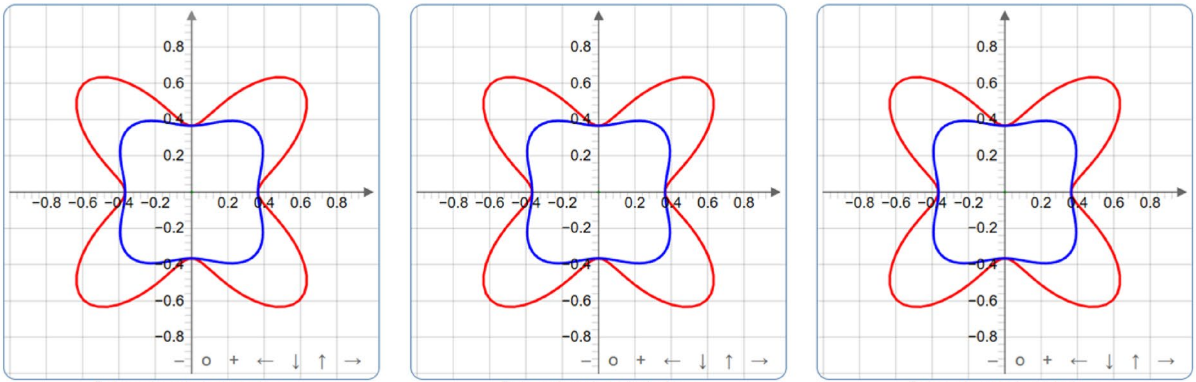

Poisson's ratio in (xy) plane Poisson's ratio in (xz) plane Poisson's ratio in (yz) plane

Fig. 5 (continued)

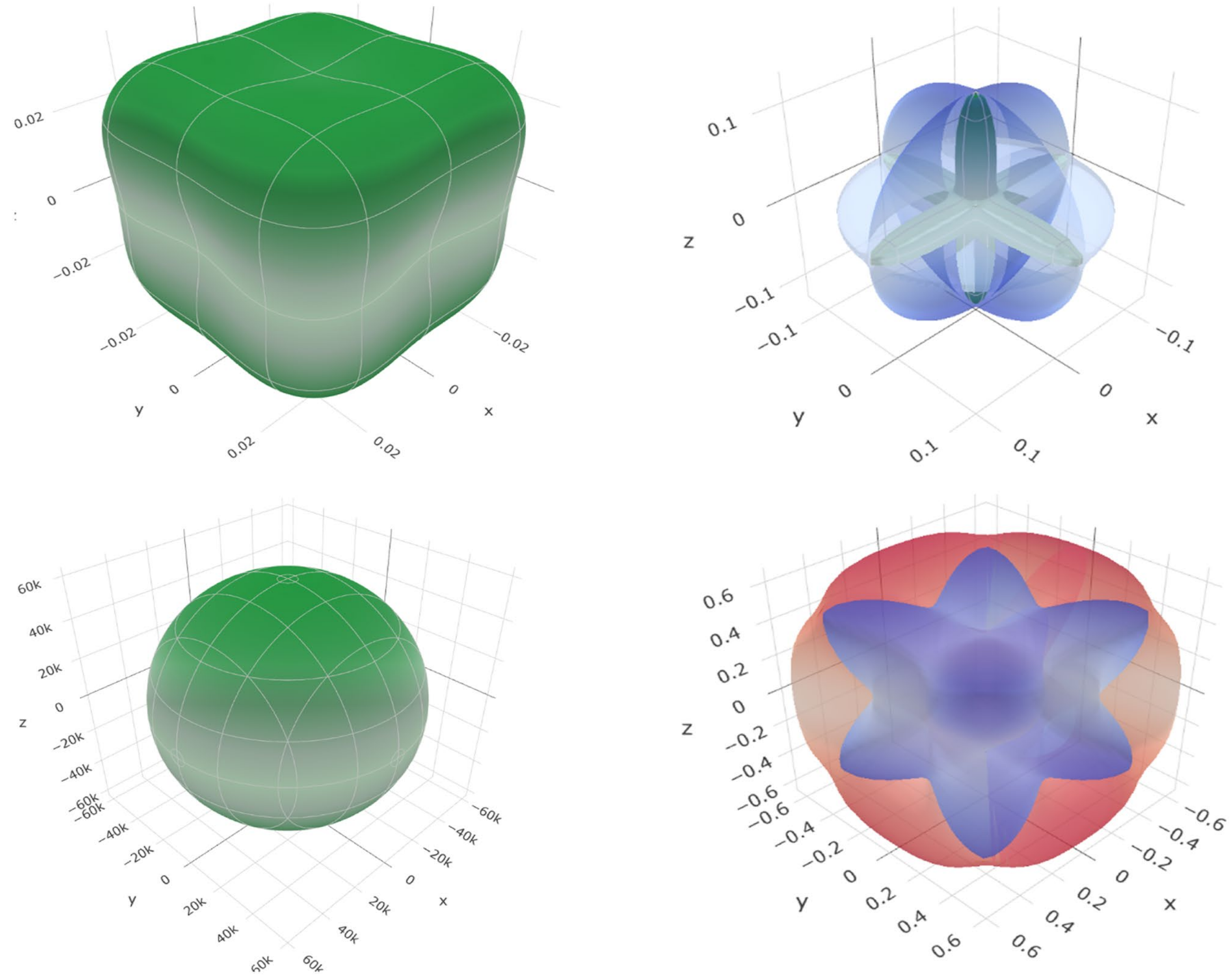

Fig. 5 (continued)

The resistance of a material, which is indicated by its stiffness, is quantified by E. Materials with higher values of E exhibit increased resistance. Therefore, as shown in Table 3, $LiMgI_3$ and $NaMgI_3$ exhibit identical and higher E values, suggesting that they possess a greater level of stiffness. The σ, which is limited to values between 0.25 and 0.50, determines the behaviour of bond forces. A value of σ greater than 0.26 indicates that the material is ductile, while a value less than 0.26 indicates that it is brittle [40]. Hence, as indicated in Table 3, the bond force of the $LiMgI_3$ and $NaMgI_3$ compounds is central (0.29). As a result, both compounds exhibited a characteristic of ductility that agrees well with the B/G ratio and Cauchy's pressure equation. Moreover, an elastic anisotropy factor (A) used to calculate the direction-dependent properties of a system. For isotropic compounds, A is ideally set at 1, indicating uniformity; any deviation from 1 signals the presence of anisotropy [19, 65]. As shown in Table 3, the computed anisotropy factors for both compounds differ from unity (0.81 for $LiMgI_3$ and 0.84 for $NaMgI_3$), indicating the presence of anisotropy in these materials. The G and B calculations allow for the determination of the transverse sound velocity, and longitudinal sound velocity, of $AMgI_3$ (A = Li/Na) crystals. The calculated Debye temperature values for $LiMgI_3$ and $NaMgI_3$ are 152.14 K and 156.04 K, respectively. Additionally, ultralow thermal conductivity values verify the thermodynamic stability of the materials under study and show that lattice

Table 4 Calculated optical properties Mg-based perovskite $AMgI_3$ (A = Li, Na) by TB-mBJ

	Property	$LiMgI_3$	$NaMgI_3$	Other work [18]
Optical properties	ε_1 (0)	3.26	3.15	3.33
	n (0)	1.80	1.77	1.92
	R (0)	0.082	0.078	0.032

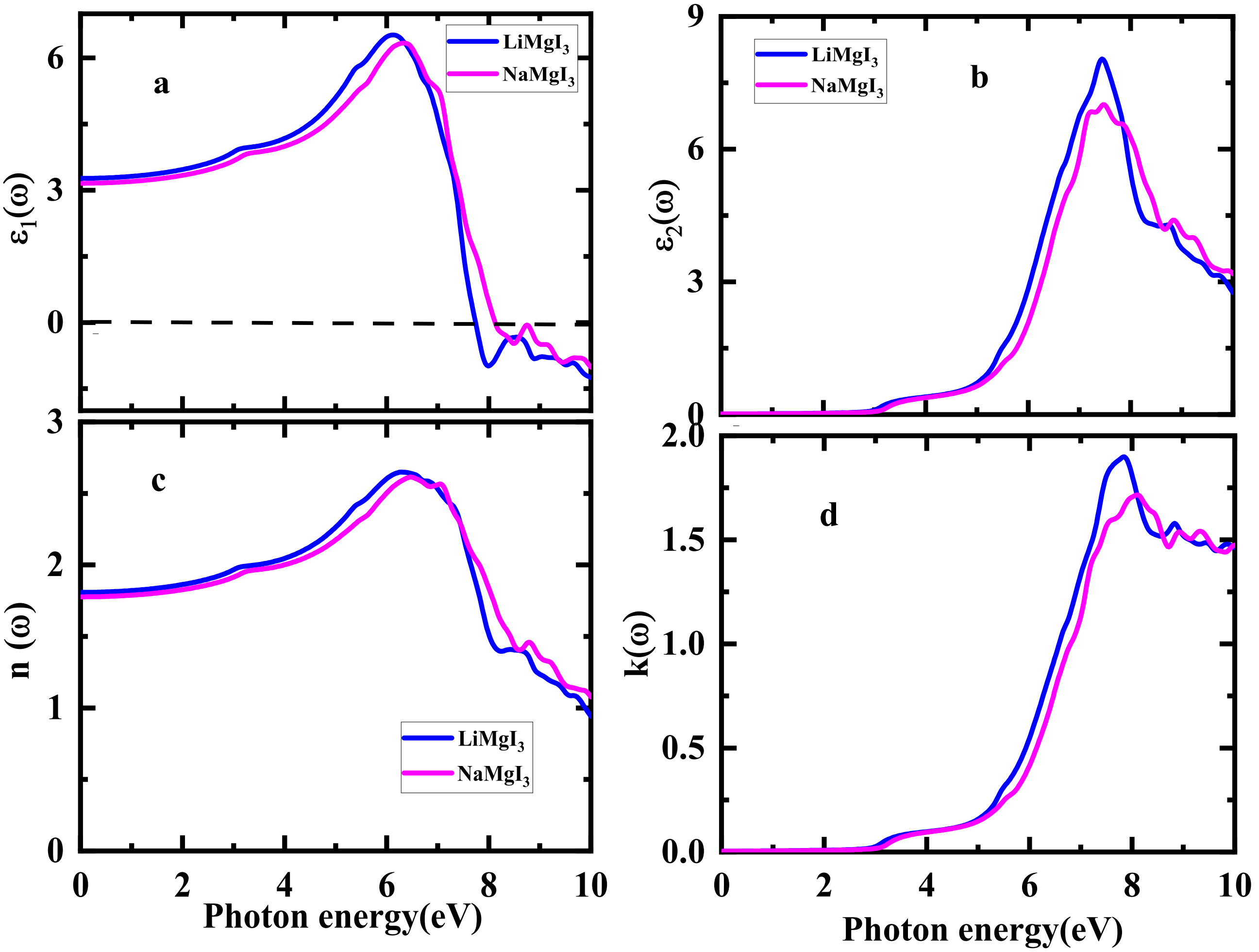

Fig. 6 Optical parameters regarding the photon energy of the compound $AMgI_3$ (A = Li, Na) **a** Real part ε_1 **b** Imaginary ε_2 **c** refractive index n, **d** extinction coefficient k (ω) optical conductivity **f** absorption coefficient **g** Reflectivity **h** energy loss function

vibration has no effect on device performance. Additionally, the hardness test revealed that compositions containing I are more dependable and resilient to applied stress [58]. The mechanical factors that were determined are shown in Table 3.

3.5 Optical Properties

These materials' optical spectra are dependent on the interaction between light and matter. Solar cells in optoelectronics transform light into electrical energy. Transitions and the rate of recombination are two crucial factors that affect this energy conversion [27, 28]. Either the light absorbs or passes through the substance. Actual dielectric constant ε1 (ω) represents light dispersion, while imaginary dielectric characteristic ε_2 (ω) represents light absorption (Table 4).

Figure 6a, b shows the dielectric functions for real and imaginary parts of $XMgI_3$ (X = Li/Na), respectively. In Fig. 6a, a static frequency of $\varepsilon_1(0)$, the real dielectric constant 3.15 for $LiMgI_3$ and 3.10 for $NaMgI_3$. The $\varepsilon_1(\omega)$ of the $LiMgI_3$ and $NaMgI_3$ reached maximum peak intensity of 6.1 eV and 6.16 eV edge of ultraviolet light region. In contrast, as shown in Fig. 6b, $LiMgI_3$ and $NaMgI_3$ revealed that 0 eV at ε_2 (0), indicating no dissipated energy exists. The imaginary part of the dielectric materials ε_2 (ω) increased until energy dissipation occurs in the photon energy absorption region. Imaginary parts of dielectric reflect the behavior of absorption coefficient. Figure 6c shows the evaluation of the optical characteristics of the refractive index, which explains the bending or refracting behavior of light in a medium. The obtained static refractive indices of $LiMgI_3$ and $NaMgI_3$ are 1.80 and 1.82, respectively. This suggests that the square of the refractive index (n(ω)) corresponds to $\varepsilon_1(\omega)$ at a static frequency, as represented in Fig. 6c. Additionally, both compounds reached their maximums at the edge of higher energy of ultra volet light (6.4 eV). The detection of refractive index peaks within the low-energy segment of the spectrum is a crucial aspect, especially in the visible

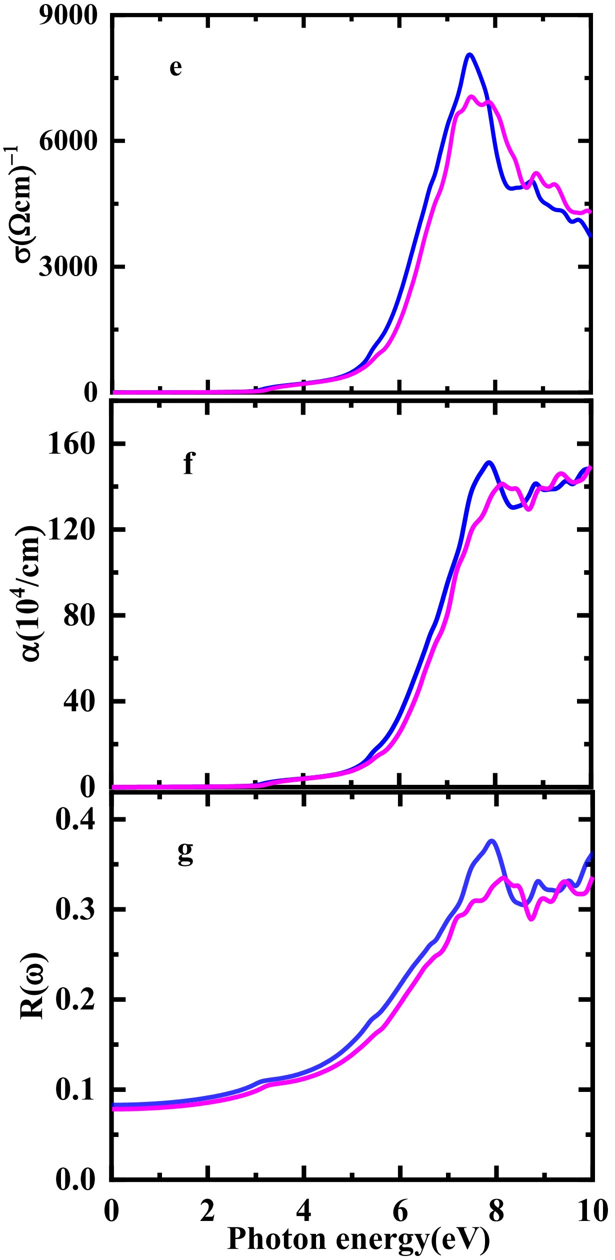

Fig. 6 (continued)

region, providing valuable insights for applications in optoelectronic devices. The extinction coefficient demonstrated how the light intensity attenuated on a given compound, $LiMgI_3$ and $NaMgI_3$, as displayed in Fig. 6d. Both compounds depicted similar behavior. Figure 6e shows how electromagnetic (EM) radiation induces the compound's optical excitation, displaying the conductivity σ (ω) of $AMgI_3$ (A = Li and Na). In $LiMgI_3$ and $NaMgI_3$, σ (ω) remains zero between 0 eV and 3.89 eV photon energy due to the absence of optical excitations, indicating no interaction between incident EM radiation and the materials' electrons in this energy range. As $LiMgI_3$ and $NaMgI_3$ absorb energy, electrons shift from the VB to the CB. Figure 6f shows the absorption coefficient of the cubic structure of $LiMgI_3$ and $NaMgI_3$. In Fig. 6f, it is evident that both $LiMgI_3$ and $NaMgI_3$ compounds initiate photon absorption at 3.6 eV and display a wide absorption peak spanning the visible to ultraviolet (UV) region. Therefore, the proposed materials are highly recommended as a novel lead-free halide perovskite material for solar harvesting applications. To comprehend the surface attributes of perovskites, examining their reflectivity offers insights. Figure 6f illustrates the reflectance spectra of $LiMgI_3$ and $NaMgI_3$ perovskite compounds relative to photon energy. Both compounds consistently demonstrate low reflectivity (less than 0.105) across the infrared to visible region spectrum, which are negligible. Remarkably, their reflectivity remains consistently low in the visible to infrared range, making these materials well-suited for solar cell applications. The spectrum's consistency with the absorption coefficient analysis Fig. 6g suggests that absorbing light within the visible part of the electromagnetic spectrum is particularly beneficial for solar cell applications (Table 4).

3.6 Thermoelectric Properties

In the present era, where the generation of the energy mainly presides on fossil fuels, requires efficient and easily manipulated substitutes that are eco-friendly in nature. The (TE) materials can be an answer with their efficient conversion of waste energy into electricity leading to the increased operating efficiency of the engines [66, 67]. The transport properties of the present materials have been calculated using the Boltzmann transport theory. We have used constant relaxation time approximation (τ) with accurate Brillouin zone (BZ) sampling with a dense grid of 1,00,000 k-points to obtain convergence. The appropriate properties for the valuable thermoelectric material require large (S), (σ/τ), (κ/τ) (PF), (zT).

To study the transport properties, we have used the tetrahedron method with energy steps of 0.16×10^4 Ry for integration. The proper selection of the energy grid majorly decides the thermoelectric properties which critically depend upon the size of the band gap of the material. Different thermoelectric parameters are plotted in Fig. 7a–f. Thermal conductivity (κ/τ) is divided into two parts: the phononic (κ_{ph}) and electronic ($\kappa_{e)}$ sections. The zT is used

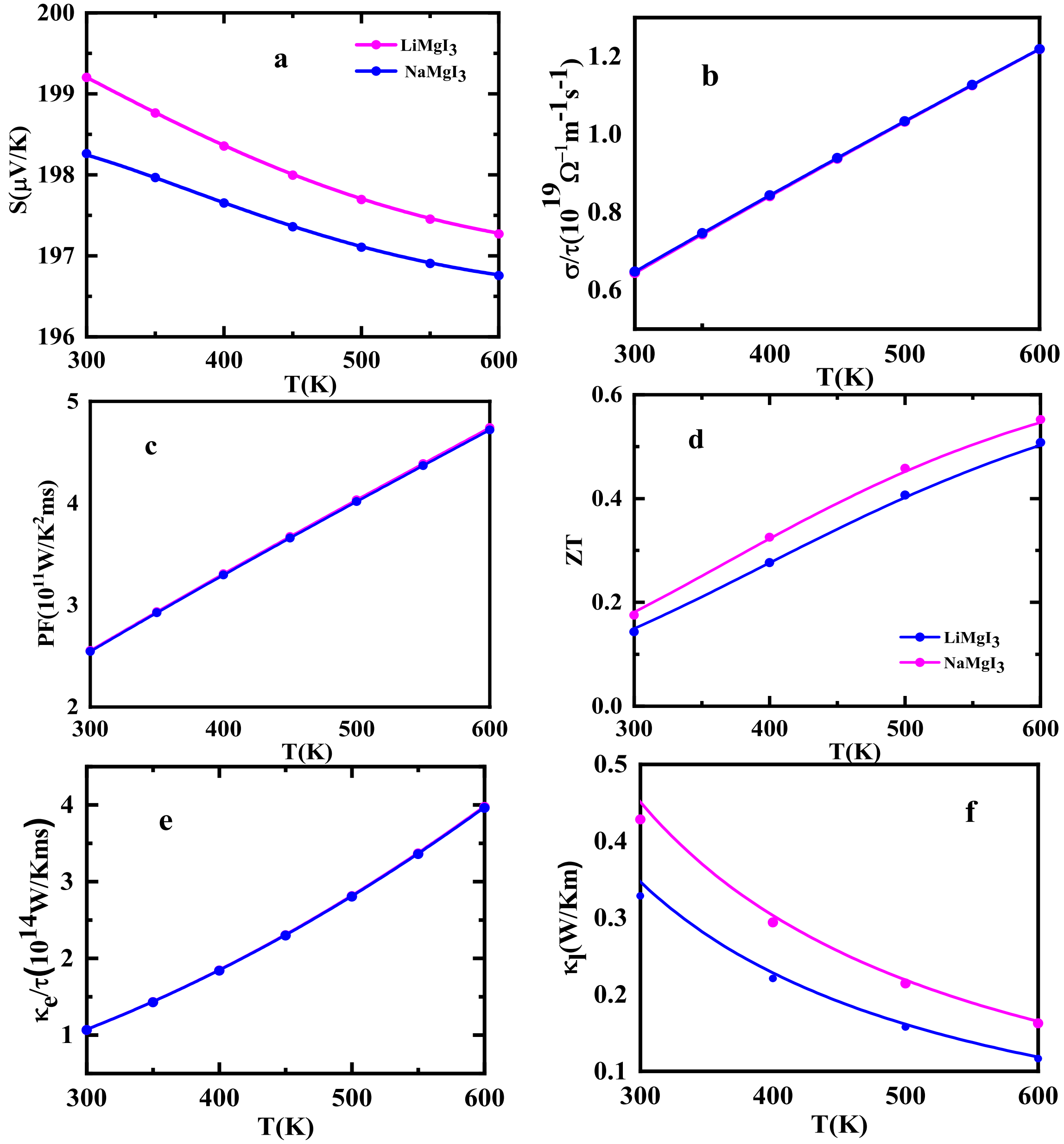

Fig. 7 Transport parameters regarding the versus temperature the TE of the compound $AMgI_3$ (A = Li, Na) **a** S, **b** σ/τ, **c** PF, **d** zT, **e** κ_e and **f** κ_l

to evaluate thermoelectric performance, and the BoltzTrap algorithm is used to calculate the κe [68].

Figure 7a. shows the Seebeck coefficient, whose value rises from 199.5/198.3 μV/K at 300 K to a maximum of 197.26/196.75 μV/K at 600 K for $LiMgI_3$($NaMgI_3$). The thermal resistive effect, which raises potential with rising temperature, could be the cause of the increases in S. Due to the smaller band gap, $LiMgI_3$ has a higher value of S than $NaMgI_3$. There are more carriers accessible at high temperatures, which explains why electrical conductivity increases with temperature [35]. As shown in Fig. 7b, at 300 K the values of electrical conductivity are 0.644×10^{19} 1/Ωms and 2.56×10^{19} 1/Ωms for (Li/Na)MgI_3. As the temperature has risen, the PF nature of both systems has directly grown. The values of PF reached 4.74×10^{11}(4.72×10^{11}) W/K^2ms at 600 K for $LiMgI_3$($NaMgI_3$) respectively (Fig. 7c). We

Table 5 Calculated transport properties of Mg-based perovskite $AMgI_3$ (A = Li, Na) at 300 K by TB-mBJ

	Material property	$LiMgI_3$	$NaMgI_3$	Other work [19]
Transport properties (300 K)	σ/τ(1018Ω^{-1} m^{-1} s^{-1})	0.644	0.648	0.54
	S(μV/K)	199	198	200
	κ_l (W/mK)	0.42	0.32	0.32
	κ_e/τ (10^{14}W/mKs)	1.07	1.07	1.00
	PF(10^{11}W/K^{2}ms)	2.55	2.55	1.99
	zT	0.14	0.17	0.54

calculated the figure of merit (zT), which is displayed in Fig. 7d. to assess performance. Up to 300 K, zT increases as temperature rises. For (Li/Na)MgI_3, the values at ambient temperature are 0.19 and 0.18, respectively. But at 600 K, the zT ratio increased by 0.50 and 0.55, which highlights the significance of the materials for thermoelectric uses.

For (Li/Na)MgI_3 systems, Fig. 7e, f. computes the electronic thermal conductivity; this allows for the calculation of lattice thermal conductivity κ_L using Slack's approach [32]. The low lattice thermal conductivity κ_L at 600 are 0.16 and 0.11 for $LiMgI_3$ and $NaMgI_3$ compounds.The transport parameters at ambient temperature are presented in Table 5.

The κ_e/τ for (Li/Na)MgI_3 systems have linear relation with the temperature, at 300 K and 600 K the value of the 3.97×10^{14}W/Kms and 3.96×10^{14}W/Kms. In semiconductors, the doping with these charge carriers intensifies the electrical conductivity and Seebeck coefficient

$$S = \frac{8\pi^2 k_B^2}{3e\hbar^2} m^* T \left(\frac{\pi}{3N}\right)^{2/3} \tag{3}$$

where N represents carrier concentration. *S* being inversely proportional to $N^{2/3}$ and it decreases with the increase in the doping carrier concentration. The μ dependence of thermoelectric properties of both the double perovskites are studied in the range of − 2.0 eV to 4.0 eV and presented in Fig. 8a, j. at different temperatures like 300 K, 700 K, 1200 K. Seebeck coefficient *S* obtained in the investigated range of temperature have positive values depicting that dominating behaviour of holes as majority charge carriers and it declines with increasing temperature. This behaviour of S again confirms the semiconducting behaviour of these compounds in Fig. 8a, b. The value of Seebeck coefficient S is found to be almost negligible in the region − 2.0 eV to 0.0 eV and it continuously rises with the chemical potential $\mu - \varepsilon_F$ and decreases with the chemical potential in the region 0.0 eV to 0.65 eV having optimal value for both n-type and p-type doping at a constant temperature. The power factor of both compounds was maximum at fermi level but here by increasing the temperature the PF increased as shown in the Fig. 8c, d.

The zT value of both perovskites' materials are approximately 1 (can be seen Fig. 8e, f) which advocates these materials are suitable for thermal devices. By increasing the temperature, the value of zT go down. For both the compounds, the electrical as well as thermal conductivities rises with that of chemical potential, illustrating the rise in their conductivities with rise in charge-carrier concentrations for both n-type and p-type doping at a fixed temperature. The value of electrical conductivity (σ/τ) is found to be maximum of $2.8\times10^{20}\Omega^{-1}m^{-1}s^{-1}$ at − 1.57 eV, which gets continuously decreases and becomes zero at 0 eV, in case of $LiMgI_3$ whereas there are two peaks $(4.5\times10^{20}\Omega^{-1}m^{-1}s^{-1})$ lying at − 1.63 eV and 0.0 eV in the n-type region demonstrated in Fig. 8g, h. The σ/τ continuously decreases with the increase in temperature whereas the κ_e/τ increases with the applied temperature in both p and n-type semiconductors, with optimal value in p region as shown in Fig. 8i, j.

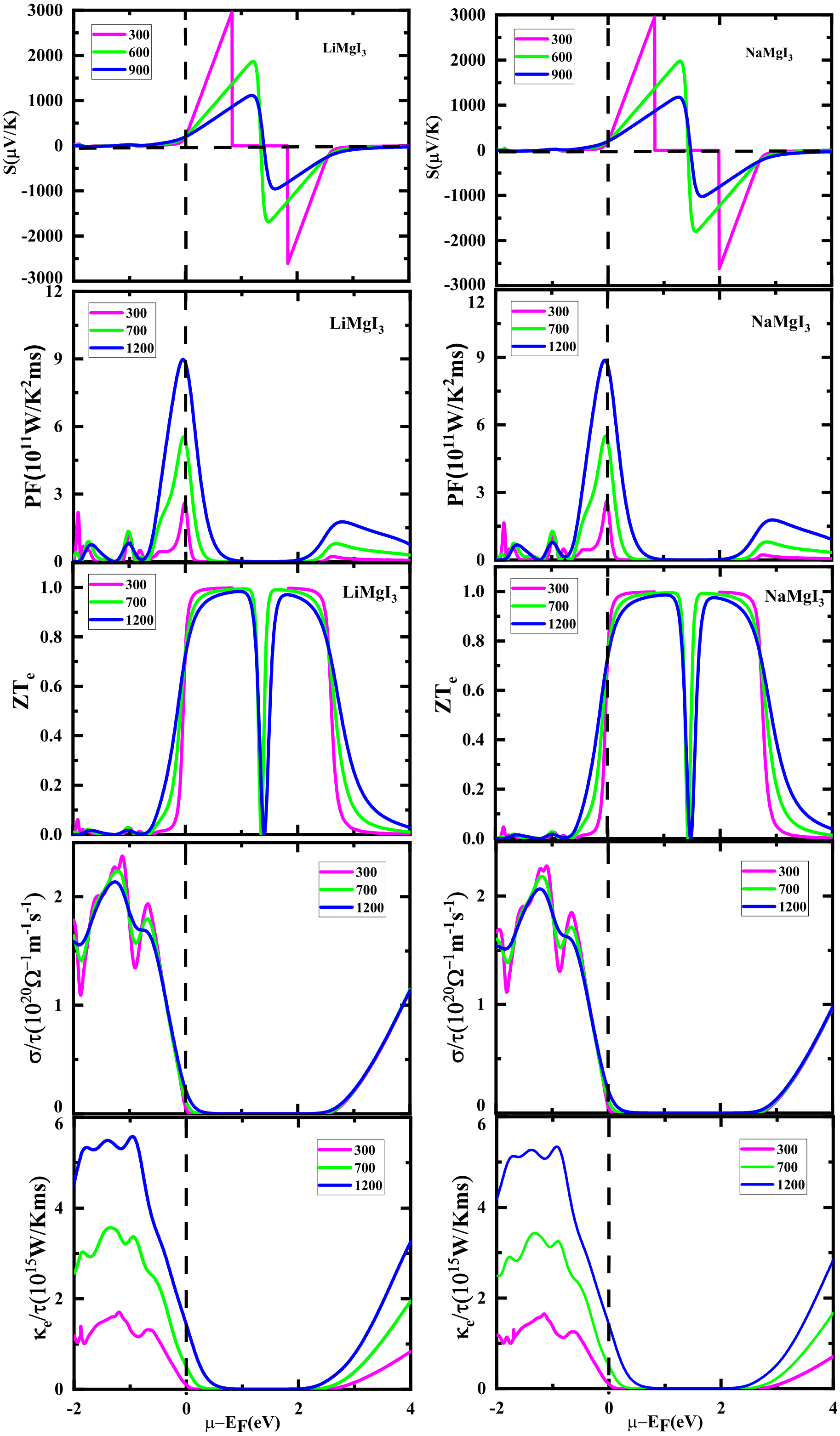

Fig. 8 Transport parameters regarding the versus chemical potential (μ) and carrier concentration (e/uc) at various temperatures (300 K, 700 K, 1200 K) for AMgI$_3$ (A = Li, Na) **a** S, **b** σ/τ, **c** PF **d** ZT **e** κ_e and **f** κ_l

4 Conclusion

This investigation explores the structural, electronic, optical, mechanical and transport attributes of cubic AMgI$_3$ (A = Li/Na) through employing WIEN2k code and BoltzTrap coding. The lattice constant (5.80 Å, 5.82 Å), ground energy (− 43130.389030 Ry, − 43440.262047 Ry) and mechanical stability were confirmed by assessing the tolerance factor (0.81, 0.87) and formation energy (– 326.60 kJ/mol, – 76.38 kJ/mol), and by evaluating the elastic constants, respectively. Our examination of the elastic constants and mechanical properties indicates the notable stability and ductile nature of each perovskite material. Additionally, we investigated the electron charge distribution using the electron localization function. The developed compounds exhibit advantageous indirect narrow band gaps (2.56 eV for $LiMgI_3$ and 2.71 eV for $NaMgI_3$) and a broad-spectrum absorption coefficient, using mBJ correlation function. The DFT analysis suggests a highly favourable band gap for photovoltaic applications. The materials $LiMgI_3$ and $NaMgI_3$ have electronic thermal conductive values of 1.07×10^{14} (W/m.K.s.), which indicates that these materials are especially appropriate for use at high temperatures. These values peak at 1200 K. Additionally, the thermoelectric component analysis shows that our materials have a favorable efficiency at ambient temperature and the possibility to increase this efficiency to higher temperatures. As a result, more work is needed to synthesis and investigate these perovskite-based substances considering upcoming advances in photovoltaic technology.

Author Contributions All persons who meet authorship criteria are listed as authors, and all authors certify that they have participated sufficiently in the work to take public responsibility for the content, including participation in the concept, design, analysis, writing, or revision of the manuscript. Mumtaz Manzoor, Anurag Tewari: Conceptualization, Methodology, Software, Writing—Original draft preparation. Ramesh Sharma, Sabah Ansar, Yedluri Anil Kumar: Writing—Original draft preparation, Visualization, Investigation. Writing—Reviewing and Editing.

Funding The authors thank the Researchers Supporting Project number (RSP2024R169), King Saud University, Riyadh, Saudi Arabia for the financial support. M.M. is supported by APVV-21-0272, VEGA-2/0070/21 project, Slovakia.

Data Availability No datasets were generated or analysed during the current study.

Declarations

Competing Interests The authors declare no competing interests.

References

1. M. Manzoor, D. Behera, S. Chowdhury, R. Sharma, M.W. Iqbal, S. Mukherjee, S.S. Alarfaji, H.A. Alzahrani, First-principles calculations to investigate structural, dynamical, thermodynamic and thermoelectric properties of CdYF3 perovskite. Comput. Theor. Chem. **1217**, 113928 (2022)
2. Y. Selmani, H. Labrim, S. Ziti, L. Bahmad, Electronic, optical and thermoelectric properties of the CsMF3 (M= Si or Ge) fluoroperovskites. Comput. Conden. Matter. **32**, e00699 (2022)
3. S. Nazir, N. Noor, M. Manzoor, A. Dahshan, Ab-initio simulations of Li-based double perovksites A2LiInBr 6 (A= Rb, Cs) for solar cell applications. Chem. Phys. Lett. **798**, 139612 (2022)
4. M. Asghar, M.W. Iqbal, M. Manzoor, N.A. Noor, M. Zanib, R. Sharma, H. Ullah, S. Aftab, T. Zahid, A computational insight of the lead-free double perovskites Rb2AgSbCl6 and Rb2AgSbBr 6 for optoelectronic and thermoelectric applications. Int. J. Energy Res. **46**, 24273–24285 (2022)
5. D. Behera, M. Manzoor, R. Sharma, M.M. Salah, I. Stich, S.K. Mukherjee, A comprehensive first-principles investigation of $SnTiO_3$ perovskite for optoelectronic and thermoelectric applications. Crystals **13**, 408 (2023)
6. Y. Selmani, H. Labrim, L. Bahmad, First-principles calculations to investigate structural, optoelectronic and thermoelectric properties of Sn-based halide perovskites: CsSnCl3 and CH3NH3SnCl3. J. Korean Ceram. Soc. **61**, 189–200 (2024)
7. M. Manzoor, D. Behera, R. Sharma, M.W. Iqbal, S.K. Mukherjee, R. Khenata, S.S. Alarfaji, H.A. Alzahrani, Investigation of the structural, mechanical, optoelectronic and thermoelectric characteristics of cubic $GeTiO_3$: an ab initio study. Mater. Today Commun. **34**, 105053 (2023)
8. Y. Selmani, H. Labrim, M. Mouatassime, L. Bahmad, Structural, optoelectronic and thermoelectric properties of Cs-based fluoroperovskites CsMF3 (M= Ge, Sn or Pb). Mater. Sci. Semicond. Process. **152**, 107053 (2022)
9. X.-G. Zhao, D. Yang, J.-C. Ren, Y. Sun, Z. Xiao, L. Zhang, Rational design of halide double perovskites for optoelectronic applications. Joule. **2**, 1662–1673 (2018)
10. S. Berri, First-principles calculations to investigate structural, electronic, elastic, optical and transport properties of halide double perovskites Cs2ABF6 (AB= BiAu, AgIr, CuBi, GaAu, InAs, InAg, InAu, InSb and InBi) for solar cells and renewable energy applications. Chem. Phys. Lett. **826**, 140653 (2023)
11. A. Babayigit, A. Ethirajan, M. Muller, B. Conings, Toxicity of organometal halide perovskite solar cells. Nat. Mater. **15**, 247–251 (2016)
12. S. Berri, Thermoelectric properties of A2BCl6: a first principles study. J. Phys. Chem. Solids **170**, 110940 (2022)
13. S. Berri, First principle analysis of structural, electronic, optical, and thermoelectric characteristics of Ba3CaTa2O9 complex perovskite. Emergent Mater. **5**, 1849–1857 (2022)
14. S. Berri, Theoretical study of physical properties of Ba3B (nb, ta) 2O9 (B= mg, ca, sr, cd, hg, zn, fe, mn, ni, co) perovskites. Comput. Conden. Matter. **29**, e00595 (2021)
15. S. Berri, Half-metallic and thermoelectric properties of Sr2EuReO6. Comput. Conden. Matter. **28**, e00586 (2021)
16. S. Berri, Theoretical analysis of the structural, electronic and optical properties of tetragonal Sr2GaSbO6. Chin. J. Phys. **55**, 2476–2483 (2017)
17. S. Berri, First-principles study on half-metallic properties of the Sr2GdReO6 double perovskite. J. Magn. Magn. Mater. **385**, 124–128 (2015)
18. M. Manzoor, M.W. Iqbal, N.A. Noor, H. Ullah, R. Sharma, S.S. Alarfaji, Exploring the structural, electronic, optical, and thermoelectric properties of potassium-based double perovskites K2AgXI6 (X= Sb, Bi) compounds: a DFT study. Mater. Sci. Eng. B **287**, 116122 (2023)
19. M. Manzoor, N. Noor, M.W. Iqbal, M. Rashid, H. Ullah, A. Dahshan, DFT study of electronic, optical, and elastic properties of double perovskites Rb2YAgX6 (X= Br, I) compounds for opto-electronic device applications. Phys. Scr. **98**, 035703 (2023)
20. M. Manzoor, M.W. Iqbal, R. Sharma, J.A. Abraham, Exploration of structural, electronic, optical, mechanical, thermoelectric, and thermodynamic properties of XInO3 (X= As, Sb) compounds for

energy harvesting applications. Int. J. Energy Res. **46**, 13409–13423 (2022)

21. H.-S. Kim, C.-R. Lee, J.-H. Im, K.-B. Lee, T. Moehl, A. Marchioro, S.-J. Moon, R. Humphry-Baker, J.-H. Yum, J.E. Moser, Lead iodide perovskite sensitized all-solid-state submicron thin film mesoscopic solar cell with efficiency exceeding 9%. Sci. Rep. **2**, 591 (2012)
22. A. Nazir, A. Dixit, E.A. Khera, M. Manzoor, R. Sharma, A. Moayad, A DFT exploration of the optoelectronic and thermoelectric features of a novel halide double perovskite A 2 YAuI 6 (A= Rb, Cs) for solar cell and renewable energy applications. Mater. Adv. **5**, 4262 (2024)
23. X. Zhang, Y. Tang, F. Zhang, C.-S. Lee, A novel aluminum–graphite dual-ion battery. Adv. Energy Mater. **6**, 1502588 (2016)
24. A. Nazir, E.A. Khera, M. Manzoor, B.A. Al-Asbahi, Y.A. Kumar, R. Sharma, A density functional theory study of the structural, mechanical, optoelectronics and thermoelectric properties of InGeX3 (X= F, Cl) perovskites. Polyhedron (2024). https://doi.org/10.1016/j.poly.2024.117009
25. M. Wang, C. Jiang, S. Zhang, X. Song, Y. Tang, H.-M. Cheng, Reversible calcium alloying enables a practical room-temperature rechargeable calcium-ion battery with a high discharge voltage. Nat. Chem. **10**, 667–672 (2018)
26. E.A. Khera, A. Nazir, M. Manzoor, M. Ayub, F. Hussain, B.A. Al-Asbahi, R. Sharma, First principles exploration of structural stability, optoelectronic and thermoelectric properties of BaXO3 (X= Hf, Ti, V) for solar cell applications. Mater. Today Commun. **39**, 108629 (2024)
27. M. Manzoor, M.W. Iqbal, I. Sadique, S.M. Wabaidur, E.A. Al-Ammar, I. Stich, R. Sharma, M.Z. Ansari, A DFT study: tailoring opto-electronic and thermoelectric performance of K2SeX6 (X= Cl, Br) double perovskites for solar cell advancements. Chin. J. Phys. **89**, 278–289 (2024)
28. M. Manzoor, M.W. Iqbal, S. Riaz, B.S. Almutairi, E.A. Khera, M. Asghar, M.Z. Ansari, R. Khenata, S. Bin-Omran, M. Aslam, First-principles calculations to investigate structural, electronic, optical and thermoelectric properties of novel double perovskite Cs2CeAgX6 (X= Cl, Br) for optoelectronic and thermoelectric applications. Chem. Phys. **575**, 112065 (2023)
29. J. Yang, J. Shang, Q. Liu, X. Yang, Y. Tan, Y. Zhao, C. Liu, Y. Tang, Variant-localized high-concentration electrolyte without phase separation for low-temperature batteries. Angew. Chem. (2024). https://doi.org/10.1002/ange.202406182
30. J. Zhang, A. Zhong, G. Huang, M. Yang, D. Li, M. Teng, D. Han, Enhanced efficiency with CDCA co-adsorption for dye-sensitized solar cells based on metallosalophen complexes. Sol. Energy **209**, 316–324 (2020)
31. M. Manzoor, D. Behera, R. Sharma, A. Moayad, A.A. Al-Kahtani, Y.A. Kumar, Comprehensive first principles to investigate optoelectronic and transport phenomenon of lead-free double perovskites Ba2AsBO6 (B= Nb, Ta) compounds. Heliyon (2024). https://doi.org/10.1016/j.heliyon.2024.e30109
32. Y. Peng, Z. Ding, G. Su, H. Hou, W. Liu, Solidification process of ABO3-type perovskites: Kinetic two-phase growth method with optimized potential. J. Mater. Sci. Technol. (2024). https://doi.org/10.1016/j.jmst.2024.03.041
33. A.I. Aljameel, G.M. Mustafa, B. Younas, H.D. Alkhaldi, G.I. Fawziah Alhajri, N.S. Ameereh, A.S. Alshomrany, Q. Mahmood, Investigation of optoelectronic and thermoelectric properties of novel for energy harvesting applications. J. Phys. Chem. Solids **189**, 111953 (2024)
34. G. Rudolph-Schöpping, E. Larsson, T.N. Pingel, M. Guizar-Sicairos, P. Villanueva-Perez, S. Hall, F. Lipnizki, Towards multiscale X-ray tomographic imaging in membrane science—a perspective. J. Membr. Sci. **690**, 122245 (2024)
35. Z. Zhang, W. Zhang, Z.-W. Hou, P. Li, L. Wang, Electrophilic halospirocyclization of N-benzylacrylamides to access 4-halomethyl-2-azaspiro [4.5] decanes. J. Org. Chem. **88**, 13610–13621 (2023)
36. C. Zhu, Optimizing and using AI to study of the cross-section of finned tubes for nanofluid-conveying in solar panel cooling with phase change materials. Eng. Anal. Boundary Elem. **157**, 71–81 (2023)
37. C. Zhu, M. Wang, M. Guo, J. Deng, Q. Du, W. Wei, Y. Zhang, S.S.A. Talesh, Optimizing solar-driven multi-generation systems: a cascade heat recovery approach for power, cooling, and freshwater production. Appl. Therm. Eng. **240**, 122214 (2024)
38. A. Fatima, S. Iqbal, T. Fazal, B. Ismail, M. Shah, A. Ayub, Q. Mahmood, N.S. Awwad, H.A. Ibrahium, F.F. Al-Fawzan, Optimization of deposition conditions of SrZrS3 perovskite thin films grown by chemical bath deposition. J. Electron. Mater. **53**, 1551–1560 (2024)
39. X. Bai, M. Xu, Q. Li, L. Yu, Trajectory-battery integrated design and its application to orbital maneuvers with electric pump-fed engines. Adv. Space Res. **70**, 825–841 (2022)
40. L. Celestine, R. Zosiamliana, S. Gurung, S.R. Bhandari, A. Laref, S. Abdullaev, D.P. Rai, A halide-based perovskite CsGeX3 (X= Cl, Br, and I) for optoelectronic and piezoelectric applications. Adv. Theory Simul. **7**, 2300566 (2024)
41. T. Cai, W. Shi, R. Wu, C. Chu, N. Jin, J. Wang, W. Zheng, X. Wang, O. Chen, Lanthanide doping into all-inorganic heterometallic halide layered double perovskite nanocrystals for multimodal visible and near-infrared emission. J. Am. Chem. Soc. (2024). https://doi.org/10.1021/jacs.3c11164
42. M.A. Sarker, M.M. Hasan, M.M. Al, A. Irfan, M.R. Islam, A. Sharif, Band gap engineering in lead free halide cubic perovskites GaGeX 3 (X= Cl, Br, and I) based on first-principles calculations. RSC Adv. **14**, 9805–9818 (2024)
43. L. Celestine, R. Zosiamliana, L. Kima, B. Chettri, Y. Singh, S. Gururng, N.S. Singh, A. Laref, D. Rai, Hybrid-DFT study of halide perovskites, an energy-efficient material undercompressive pressure for piezoelectric applications. J. Phys. Condens. Matter (2024). https://doi.org/10.1088/1361-648X/ad443e
44. S. Jamshaid, M.R. Cicconi, W. Heiss, K.G. Webber, P.J. Wellmann, Synthesis and characterization of BaZrS3 thin films via stacked layer methodology: a comparative study of BaZrS3 on zirconium foil and silicon carbide substrates. Adv. Eng. Mater. (2024). https://doi.org/10.1002/adem.202302161
45. T. Demkiv, Y. Chornodolskyy, T. Muzyka, S. Malynych, R.Y. Serkiz, A. Pushak, A. Kotlov, R. Gamernyk, Effect of Yb doping on the optical and photoelectric properties of CsPbCl3 single crystals. Opt. Mater.: X. **22**, 100303 (2024)
46. Y. Ju, W. Liu, Z. Zhang, R. Zhang, Distributed three-phase power flow for AC/DC hybrid networked microgrids considering converter limiting constraints. IEEE Trans. Smart Grid. **13**, 1691–1708 (2022)
47. E. Jain, G. Pagare, S.S. Chouhan, Full potential linearized augmented plane wave (FP-LAPW) study of intermetallic compound: BeCu. Int. J. Adv. Electron. Comput. Eng. **3**, 306–309 (2014)
48. M. Zanib, M. Manzoor, N. Noor, M.W. Iqbal, M. Asghar, H. Hegazy, A. Laref, DFT investigation of half-metallic ferromagnetic rare earth based spinels MgHo2Z4 (Z= S, se). J. Rare Earths (2023). https://doi.org/10.1016/j.jre.2023.02.002
49. P. Blaha, K. Schwarz, G. Madsen D. Kuasnicke, J. Luitz, *Introduction to WIEN2K*, An augmented plane wane plus local orbitals program for calculating crystal properties (Vienna university of technology, Vienna, Austria, 2001) (2001)
50. P. Blaha, K. Schwarz, G.K. Madsen D. Kvasnicka, J. Luitz *wien2k*, An augmented plane wave+ local orbitals program for calculating crystal properties. **60** (2001)

51. P. Blaha, K. Schwarz, F. Tran, R. Laskowski, G.K. Madsen, L.D. Marks, WIEN2k: An APW+ lo program for calculating the properties of solids. J. Chem. Phys. **152**, 074101 (2020)
52. M. Siddique, A.U. Rahman, A. Iqbal, B.U. Haq, S. Azam, A. Nadeem, A. Qayyum, A systematic first-principles investigation of structural, electronic, magnetic, and thermoelectric properties of thorium monopnictides Th Pn (Pn= N, P, As): a comparative analysis of theoretical predictions of LDA, PBEsol, PBE-GGA, WC-GGA, and LDA+ U methods. Int. J. Thermophys. **40**, 1–21 (2019)
53. M. Bezzerrouk, M. Hassan, R. Baghdad, S. Reguieg, M. Bousmaha, B. Kharroubi, B. Bouhafs, Thermodynamic, structural and electronic, properties of SnO2: By GGA and GGA+ trans-blaha-modified Becke-Johnson (TB-mBJ) calculation. Superlattices Microstruct. **84**, 80–90 (2015)
54. G.K. Madsen, D.J. Singh, BoltzTraP. A code for calculating band-structure dependent quantities. Comput. Phys. Commun. **175**, 67–71 (2006)
55. C.J. Bartel, J.M. Clary, C. Sutton, D. Vigil-Fowler, B.R. Goldsmith, A.M. Holder, C.B. Musgrave, Inorganic halide double perovskites with optoelectronic properties modulated by sublattice mixing. J. Am. Chem. Soc. **142**, 5135–5145 (2020)
56. H. Murtaza, Q. Ain, J. Munir, H.M. Ghaithan, A.A.A. Ahmed, A.S. Aldwayyan, S.M. Qaid, Effect of bandgap tunability on the physical attributes of potassium-based K2CuBiX6 (X= I, Br, Cl) double perovskites for green technologies. Inorg. Chem. Commun. **162**, 112206 (2024)
57. H. Murtaza, Q. Ain, J. Munir, H.M. Ghaithan, M. Ali, A.A.A. Ahmed, S.M. Qaid, Tuning the thermoelectric and optoelectronic attributes of lead-free novel fluoroperovskites Cs2BB’F6 (B= Rb, In, Na and B’= Ir, As, Rh): A first-principles investigation. J. Phys. Chem. Solids **190**, 111934 (2024)
58. K. Frohna, T. Deshpande, J. Harter, W. Peng, B.A. Barker, J.B. Neaton, S.G. Louie, O.M. Bakr, D. Hsieh, M. Bernardi, Inversion symmetry and bulk Rashba effect in methylammonium lead iodide perovskite single crystals. Nat. Commun. **9**, 1829 (2018)
59. K. Boudiaf, A. Bouhemadou, O. Boudrifa, K. Haddadi, F.S. Saoud, R. Khenata, Y. Al-Douri, S. Bin-Omran, M. Ghebouli, Structural, elastic, electronic and optical properties of LaOAgS-type silver fluoride chalcogenides: first-principles study. J. Electron. Mater. **46**, 4539–4556 (2017)
60. S.A. Dar, R. Sharma, V. Srivastava, U.K. Sakalle, Investigation on the electronic structure, optical, elastic, mechanical, thermodynamic and thermoelectric properties of wide band gap semiconductor double perovskite Ba 2 InTaO 6. RSC Adv. **9**, 9522–9532 (2019)
61. A. Khireddine, A. Bouhemadou, S. Maabed, S. Bin-Omran, R. Khenata, Y. Al-Douri, Elastic, electronic, optical and thermoelectric properties of the novel Zintl-phase Ba2ZnP2. Solid State Sci. **128**, 106893 (2022)
62. L. Zuo, M. Humbert, C. Esling, Elastic properties of polycrystals in the Voigt-Reuss-Hill approximation. J. Appl. Crystallogr. **25**, 751–755 (1992)
63. Z. Souadia, A. Bouhemadou, R. Khenata, Y. Al-Douri, Structural, elastic and lattice dynamical properties of the alkali metal tellurides: first-principles study. Physica B **521**, 204–214 (2017)
64. N.U. Khan, U.A. Khan, A. Zaman, A. Algahtani, J.Y. Al-Humaidi, V. Tirth, A.M. Alsuhaibani, T. Al-Mughanam, M.S. Refat, A. Ali, Insight to structural, electronic, optical and elastic properties of double perovskites Rb2XCrCl6 (X= K, Na) via DFT study. J. Phys. Chem. Solids **181**, 111479 (2023)
65. L. Dong, S. Sun, Z. Deng, W. Li, F. Wei, Y. Qi, Y. Li, X. Li, P. Lu, U. Ramamurty, Elastic properties and thermal expansion of lead-free halide double perovskite Cs2AgBiBr 6. Comput. Mater. Sci. **141**, 49–58 (2018)
66. M. Manzoor, M. Hussain, M. Aslam, B. Evgeny, R. Sharma, A.S. Alshomrany, N. Sfina, Tailoring the physical, optoelectronic and transport properties of novel lead-free Sodium perovskites Na2TeX6 (X= Cl, Br, I) using DFT computation for photovoltaic and thermal devices. Chin. J. Phys. (2024). https://doi.org/10.1016/j.cjph.2024.02.027
67. B. Beltrán-Pitarch, J. Prado-Gonjal, A.V. Powell, P. Ziolkowski, J. García-Cañadas, Thermal conductivity, electrical resistivity, and dimensionless figure of merit (ZT) determination of thermoelectric materials by impedance spectroscopy up to 250 C. J. Appl. Phys. (2018). https://doi.org/10.1063/1.5036937
68. N. Kojal, S. Javec, Structural and thermal properties of H6Ta2O17. Exp. Theor. Nanotechnol. (2023). https://doi.org/10.56053/7.2.309
69. M. Manzoor, D. Bahera, R. Sharma, F. Tufail, M.W. Iqbal, S.K. Mukherjee, Investigated the structural, optoelectronic, mechanical, and thermoelectric properties of Sr2BTaO6 (B= Sb, Bi) for solar cell applications. Int. J. Energy Res. **46**, 23698–23714 (2022)